

1 **Using one-step facile and solvent-free mechanochemical process to synthesize photoactive**
2 **Fe₂O₃-TiO₂ in treatment of industrial wastewater**

3

4 Wennie Subramonian, Ta Yeong Wu* and Siang-Piao Chai

5

6 Chemical Engineering Discipline, School of Engineering, Monash University, Jalan Lagoon
7 Selatan, 47500 Bandar Sunway, Selangor Darul Ehsan, Malaysia.

8

9 *Corresponding author: Ta Yeong Wu

10 E-mail addresses: wu.ta.yeong@monash.edu; tayeong@hotmail.com

11 Tel.: +60 3 55146258

12 Fax: +60 3 55146207

13

14 **ABSTRACT**

15

16 In this present study, Fe₂O₃-TiO₂ photocatalyst was synthesized and used to degrade real
17 industrial wastewater, namely pulp and paper mill effluent (PPME). Fe₂O₃-TiO₂ was synthesized
18 via ball milling at ambient conditions without incorporating any solvent. Comprehensive
19 characterization studies and photocatalytic evaluations of the synthesized Fe₂O₃-TiO₂ were
20 conducted in this study. It was verified that Fe₂O₃-TiO₂ possessed crystalline structures of γ -
21 Fe₂O₃, anatase and rutile TiO₂. Also, a good dispersion of Fe and O elements within the TiO₂
22 framework could be attained. A detection of Fe-O-Ti bond elucidated a substitution of Ti⁴⁺ by
23 Fe³⁺ in the TiO₂ lattice sites through mechanical milling, which ultimately enhanced the

24 photocatalytic activities of Fe₂O₃-TiO₂. Moreover, Fe₂O₃-TiO₂ exhibited enhanced catalytic
25 properties in terms of specific surface area (58.40 m²/g), porosity (0.29 cm³/g), band gap (2.95
26 eV), and charge separation in comparison with commercial P25. The present work also proved
27 that both characteristics and photoactivity of Fe₂O₃-TiO₂ were significantly affected by its
28 synthesis conditions (milling time, milling speed, and Fe₂O₃ loading). The highest treatment
29 efficiency of PPME (62.3% of chemical oxygen demand or COD removal) was achieved using
30 Fe₂O₃-TiO₂, which was synthesized at 20 min, 250 rpm and 1 mol% of milling time, milling
31 speed and Fe₂O₃ loading, respectively. Noticeably, the photoactivity of the Fe₂O₃-TiO₂ was more
32 superior than the P25 (40.6% of COD removal). This study proved that mechanochemical
33 process enabled the green synthesis of Fe₂O₃-TiO₂ that could be used in treatment of real
34 industrial wastewater.

35

36 **Keywords:** Ball milling; Iron (III) oxide; Titanium (IV) oxide; Photocatalysis; Pulp and paper
37 mill effluent; Wastewater treatment

38

39 1. Introduction

40

41 Pulp and paper mills are one of the major sources of industrial pollution worldwide, in
42 which pulp and paper effluent (PPME) contains high amount of total suspended solids, chemical
43 oxygen demand (COD), and other toxic contaminants [1]. However, most PPME treatment
44 plants apply biological treatment systems, which result in ineffective removal of colour and
45 toxicity from the effluent [2]. As an alternative, advanced oxidation processes (AOPs) have been
46 proposed in wastewater treatment systems to effectively oxidize recalcitrant pollutants into
47 biodegradable intermediates and innocuous compounds (i.e. carbon dioxide and water) due to the
48 generation of highly potent oxidant, hydroxyl radicals ($\cdot\text{OH}$) [3,4]. Other advantages of AOPs
49 include colour removal from the wastewater, lower sludge production, and simplicity in
50 operation [5]. Among several AOPs, powerful oxidants such as ozone, hydrogen peroxide, and
51 potassium permanganate have been studied in photocatalysis of wastewater. Typically, these
52 oxidants were used in homogenous photocatalysis processes, which incurred instability and
53 difficulty in catalyst separation process [6]. Conversely, heterogeneous photocatalysis is deemed
54 as the most economically profitable and environmentally safe technology among other AOPs in
55 the removal of organic pollutants from water systems [7]. Hence, heterogeneous photocatalysis
56 was employed as a promising treatment route to degrade highly contaminated PPME in this
57 current study.

58 Numerous studies have established that TiO_2 as one of the most promising photocatalysts to
59 initiate photocatalytic reactions, owing to its optical and electronic properties, strong oxidizing
60 power, chemical inertness, high stability, non-toxicity, corrosion resistant, inexpensiveness, and
61 environmentally benign nature as compared to other photocatalysts [8-10]. However, TiO_2 has a

62 wide band gap (anatase phase: 3.2 eV and rutile phase: 3.0 eV) and presents a high
63 recombination rate of photogenerated electron-hole pairs [11,12]. In view of this, coupling of
64 TiO₂ with other metal oxides (e.g. Fe₂O₃ [13], WO₃ [14], ZnO [15], SnO₂ [16], and CeO₂ [17])
65 was investigated extensively for its potential application in degradation of organic pollutants.
66 Generally, the synthesis of these hybrid metal oxides photocatalysts employed conventional
67 methods (such as sol-gel, hydrothermal, solvothermal, precipitation, and chemical/physical
68 vapour deposition) that posed several drawbacks. These conventional methods were
69 predominantly multi-step procedures, necessitated the utilization of toxic metal-organic
70 precursors, and required expensive equipment [18,19]. Also, longer duration was needed, which
71 was undesirable for industrial fabrication purposes [18]. Therefore, development of a greener and
72 facile fabrication method using non-solvent synthesis under ambient temperature and
73 atmospheric pressure was pursued in the current work.

74 Green chemistry was an initiative driven by the U.S. Environmental Protection Agency in
75 the early 1990. It involved the design of chemical products and processes that reduced or
76 eliminated the need and generation of hazardous substances [20]. Growing emphasis on green
77 chemistry led to the use of mechanochemical process as a prospective method to activate and
78 fabricate a photocatalyst under a solvent-free condition [21]. Previously, mechanochemical
79 reaction was applied widely in areas including material synthesis, coal industry, extractive
80 metallurgy, powder surface modification, pharmacy, and waste management [22]. During the
81 course of mechanochemical process via ball milling (mechanical milling), accumulated potential
82 energy with shear and friction forces were transferred from milling balls to the materials. This
83 energy induced severe plastic deformation as well as created new interfaces and defects on the
84 materials, which potentially led to substantial improvement in material properties of the final

85 product [23-25]. Mechanochemical process has gained importance over conventional synthesis
86 methods because of its greener and facile technique [8,18]. In comparison with conventional
87 synthesis methods, mechanochemical process did not require solvents and thus, no wastes were
88 generated from catalyst washing. It also eliminated the need of multi-step procedures, high
89 temperature and pressure conditions, plus no additions of hazardous and expensive chemicals
90 were required [25,26]. Moreover, mechanochemical process yielded large quantities of desired
91 product at ambient conditions within a very short processing time [8,18]. The advantages from
92 this process serve as a very lucrative aspect from an economical viewpoint, thus, making
93 mechanochemical synthesis very attractive for large-scale industrial production [18].

94 Herein, the current study demonstrated a facile and solvent-free mechanochemical process
95 via mechanical milling to synthesize $\text{Fe}_2\text{O}_3\text{-TiO}_2$ photocatalyst as an approach towards a greener
96 process. The synthesized $\text{Fe}_2\text{O}_3\text{-TiO}_2$ was used in degrading real PPME. To the best of our
97 knowledge, there has been no report concerning the use of mechanochemically fabricated $\text{Fe}_2\text{O}_3\text{-}$
98 TiO_2 photocatalyst in treating real industrial effluent, such as PPME. Thus, a detailed
99 characterization study was performed to closely examine the structural and textural properties of
100 the fabricated $\text{Fe}_2\text{O}_3\text{-TiO}_2$ via mechanochemical process. To further understand
101 mechanochemical process, effects of fundamental synthesis conditions (i.e. milling time, milling
102 speed, and Fe_2O_3 loading) on the properties and photoactivity of $\text{Fe}_2\text{O}_3\text{-TiO}_2$ were studied.

103

104

105

106

107

108 2. Experimental details

109

110 2.1. Materials

111 Iron (III) oxide, tungsten (VI) oxide, zinc oxide, cerium (IV) oxide, anatase titanium (IV)
112 oxide, rutile titanium (IV) oxide, and Aeroxide[®] P25 were purchased from Sigma-Aldrich. All
113 chemicals were used as received without further modification. Raw PPME was collected from
114 Muda Paper Mills Sdn. Bhd., Kajang, Selangor. According to Subramonian et al. [27], raw
115 PPME should be pre-treated using coagulation process to reduce the amount of total suspended
116 solids from the effluent. In this study, PPME was pre-treated to the methods proposed by
117 Subramonian et al. [28] and the pre-treated PPME with lesser suspended solids was used to
118 evaluate the photocatalytic performance of the synthesized Fe₂O₃-TiO₂.

119

120 2.2. Mechanochemical synthesis of Fe₂O₃-TiO₂

121 Fe₂O₃-TiO₂ photocatalyst was fabricated in the absence of solvent via mechanochemical
122 process using a planetary ball mill (Fritsch Pulverisette 5). Two zirconia vials with 500 cm³
123 capacity were filled with a stoichiometric amount of Fe₂O₃ and P25 powder. 10 mm diameter
124 balls were used as milling medium. Ball to powder mass ratio was kept constant at 10:1. Effect
125 of mechanochemical synthesis conditions on the fabricated photocatalyst was studied by varying
126 the milling time (10-30 min), milling speed (150-350 rpm), and Fe₂O₃ molar content (0.4-1.2
127 mol%). The synthesized Fe₂O₃-TiO₂ was then characterized and its catalytic performance was
128 evaluated based on COD removal of PPME.

129

130 2.3. Characterization study

131 Crystallinity and phase identification of samples were determined from powder X-ray
132 diffraction (XRD) patterns. XRD data was recorded on a X-ray diffractometer (Bruker D8
133 Discovery) using Ni filtered Cu-K α radiation ($\lambda = 0.154056$ nm) at a scan rate of $0.02^\circ \text{ s}^{-1}$. The
134 accelerating voltage and current were 40 kV and 40 mA, respectively. Crystallite sizes of the
135 samples were calculated based on Scherrer formula. Surface morphology and elemental
136 compositions of the samples were obtained using field electron scanning electron spectroscopy
137 (FESEM) (Hitachi SU8010) equipped with energy-dispersive X-ray (EDX). X-ray photoelectron
138 spectroscopy (XPS) analysis was conducted on a Kratos Axis-Ultra DLD instrument with a
139 monochromatized Al K α X-ray source (15 kV, 200 W) at a pressure of 7.6×10^{-9} Torr and 20 eV
140 pass energy. All binding energies were referenced to C 1s peak at 284.6 eV of the adventitious
141 carbon. Transmission electron microscopy (TEM) images were taken with a JEOL JEM-2100F
142 microscope operated at 200 kV. Meanwhile, textural properties of the samples were analyzed
143 based on nitrogen adsorption/desorption isotherms using Micromeritics, ASAP 2020. Specific
144 surface areas and pore distributions were determined from Brunauer-Emmett-Teller (BET) and
145 Barrett-Joyner-Halenda (BJH) methods, respectively. Raman spectra were acquired using
146 HORIBA Scientific, LabRAM HR Evolution with an excitation wavelength of 514 nm under
147 room temperature whereas Fourier transform infrared (FTIR) spectra were recorded over a range
148 of $4000\text{-}400 \text{ cm}^{-1}$ at room temperature using a FTIR spectrophotometer (Thermo Scientific
149 Nicolet iS10). Additionally, ultraviolet-visible (UV-vis) diffused reflectance spectra (DRS) were
150 recorded on a UV-vis spectroscopy (Cary 100, Agilent) with BaSO $_4$ as reference. Band gap
151 energies of the samples were estimated from plot of transformed Kubelka-Munk function $[F(R)$
152 $\cdot hv]^{1/2}$ against abscissa of photon energy (hv). Photoluminescence (PL) emission spectra was

153 analyzed using a fluorescence spectrometer (LS55, Perkin Elmer) at an excitation wavelength of
154 315 nm with 500 nm min⁻¹ scanning speed. The widths of the excitation and emission slits were
155 fixed at 10 nm.

156

157 **2.4. Photocatalytic evaluation of Fe₂O₃-TiO₂**

158 Photoactivity of the prepared Fe₂O₃-TiO₂ was evaluated in terms of photodegradation of
159 PPME. In a typical procedure, 1.0 g/L of Fe₂O₃-TiO₂ was dispersed in 50 mL of PPME at pH 4.
160 The suspension was magnetically stirred in the dark at 800 rpm for 30 min to achieve adsorption-
161 desorption equilibrium. Then, the suspension was exposed to UV irradiation (400 W of UV
162 lamp) for 3 h under continuous stirring and aeration (air flow rate = 4.0 L/min). The initial and
163 final samples were withdrawn from the suspension before and after irradiation to determine a
164 change in COD (Equation (1)). Photocatalyst was removed from the samples by centrifugation
165 (13500 rpm for 15 min).

$$166 \quad COD \text{ removal, \%} = \frac{COD_{initial} - COD_{final}}{COD_{initial}} \times 100 \quad (1)$$

167

168

169 **3. Results and discussion**

170

171 **3.1. Effect of mechanical milling on characteristics and photoactivity of Fe₂O₃-TiO₂**

172 In mechanochemical synthesis, metal oxide powders (Fe₂O₃ and TiO₂) were plastically
173 deformed due to high-energy impact between milling balls and wall of the vial, producing the
174 final composite Fe₂O₃-TiO₂ [8]. Fundamental mechanochemical synthesis conditions played a
175 crucial role in manipulating photocatalytic properties of Fe₂O₃-TiO₂ [7]. Therefore, the present

176 study investigated the effect of mechanochemical process conditions (milling time, milling
177 speed, and loading of Fe_2O_3) on the intrinsic properties and photoactivity of Fe_2O_3 - TiO_2 .

178

179 **3.1.1. Effect of milling time**

180 Change in Fe_2O_3 - TiO_2 morphology as a function of milling time was observed from FESEM
181 images. Mechanically milled Fe_2O_3 - TiO_2 samples were gradually ground to finer particles from
182 10 to 20 min (Fig. 1a-c) due to longer duration of impact and shear forces incurred from the
183 milling balls. However, prolonging the milling time above 20 min resulted in highly
184 agglomerated particles with rough surfaces (Fig. 1d and e). Similar findings were observed by
185 House et al. [29]. Powder that was milled at 25 and 30 min had a high surface energy, which
186 facilitated the powder to reunite and reaggregate in order to reduce surface energy and re-
187 stabilize the system [30]. In short, fracture of solids only occurred at shorter milling time
188 whereas reagglomeration appeared at longer milling time [31]. Surface morphology of Fe_2O_3 -
189 TiO_2 , P25 and Fe_2O_3 powder were also compared. From the FESEM images, P25 powder (Fig.
190 1f) consisted of uniform spherical particles whereas Fe_2O_3 (Fig. 1g) particles were large and
191 irregular-sized. The fabricated Fe_2O_3 - TiO_2 (Fig. 1a-c) photocatalyst was finer than Fe_2O_3 (Fig.
192 1g). In addition, Fe_2O_3 - TiO_2 (Fig. 1a-c) was irregular in shape, randomly organized, and slightly
193 agglomerated as compared to P25 (Fig. 1f). Carneiro et al. [8] also reported very similar catalyst
194 morphology that was induced by the effect of ball milling.

195 An employment of mechanochemical synthesis was reported to promote mesoporosity and
196 change in specific surface area of the materials [32]. Hence, surface properties of the synthesized
197 Fe_2O_3 - TiO_2 were evaluated at different milling time and were compared with Fe_2O_3 and pristine
198 P25. According to IUPAC classification, nitrogen adsorption/desorption isotherm of Fe_2O_3 - TiO_2

199 showed a typical type IV pattern with a hysteresis loop beginning around relative pressure of 0.7
200 (Fig. 2). The pattern suggested the occurrence of mesoporous structure with a broad pore size
201 distribution [32,33]. Pore size distribution curve (inset in Fig. 2) depicts a wide range of pore
202 diameter from 4 to 35 nm with the pore size mainly distributed at 17 nm, implying that an
203 incorporation of Fe_2O_3 into TiO_2 lattice through mechanochemical synthesis did not defect the
204 surface mesoporous structure of the TiO_2 [34]. Specific surface area, pore volume, and pore size
205 of Fe_2O_3 - TiO_2 were found to be higher than P25 (Table 1). Higher textural properties provided
206 better surface adsorption and mass transfer between organic pollutants and Fe_2O_3 - TiO_2 in the
207 catalyst pore, suggesting a potential enhancement in photocatalytic activity [34].

208 The specific surface areas, pore volumes, and pore sizes of the milled samples were also
209 clearly affected by the milling time (Table 2). Overall, the aforementioned textural properties
210 improved from milling time 10 to 20 min because of repeated fracturing of solids induced by the
211 milling balls, which consequently led to a reduction in particle size, and an increase in both
212 surface area and porosity [31]. However, a deterioration of textural properties occurred from 25
213 to 30 min due to reagglomeration of solids as evidenced in Fig. 1d and e. Similarly, the
214 photocatalytic trend also displayed a gradual increase in COD removal (52.7 to 62.3%) from 10
215 to 20 min, followed by a decrease (57.4 to 52.8%) from 25 to 30 min of milling time (Fig. 3).
216 One-way analysis of variance (ANOVA) revealed that the recommended milling time was 20
217 min. Thus, subsequent synthesis of Fe_2O_3 - TiO_2 photocatalyst was carried out based on this
218 milling time.

219

220 3.1.2. Effect of milling speed

221 Change in milling speed stimulated modifications to the crystallite structure of $\text{Fe}_2\text{O}_3\text{-TiO}_2$.
222 It was proven in this study that by increasing the milling speed (150 to 350 rpm), XRD
223 diffraction peaks (Fig. 4) became broader with diminishing intensities. The result denoted the
224 presence of smaller-sized particles formed at elevated milling speed [8]. Besides, crystallite sizes
225 of $\text{Fe}_2\text{O}_3\text{-TiO}_2$ also decreased with increasing milling speed (150 to 350 rpm) as shown in Table
226 3. Mechanical impact from the milling balls at rising milling speed deformed the powders and
227 introduced lattice defects, leading to a reduction in crystallite size [8]. Fig. 5 shows an
228 improvement in catalytic activity from 150 to 250 rpm (52.2 to 62.3% of COD removal,
229 respectively) followed by a drop from 300 to 350 rpm (53.2 to 50.2% of COD removal,
230 respectively). Decline in photoactivity at elevated milling speed was attributed to higher rutile
231 content in $\text{Fe}_2\text{O}_3\text{-TiO}_2$ at 300 to 350 rpm (Table 3). The rutile phase fraction for each sample
232 (Table 3) was determined from the XRD patterns (Fig. 4) using Spurr equation. At higher milling
233 speed, more collisions occurred between the milling balls and powders. Following that, an
234 increase of local temperature and pressure at the collision sites induced an anatase-to-rutile phase
235 transformation of the fabricated $\text{Fe}_2\text{O}_3\text{-TiO}_2$ [8]. One-way ANOVA suggested that 250 rpm was
236 the recommended milling speed to prepare $\text{Fe}_2\text{O}_3\text{-TiO}_2$ and subsequent milling was carried out
237 using this speed.

238 In addition, XRD patterns of the synthesized $\text{Fe}_2\text{O}_3\text{-TiO}_2$ (Fig. 4) exhibited characteristic
239 peaks of Fe_2O_3 , anatase, and rutile TiO_2 . Peaks at 25.3, 37.8, 48.1, 54.4, 55.1, 62.7, 69.0, and
240 75.1° corresponded to (101), (004), (200), (105), (211), (204), (116), and (215) planes,
241 respectively of anatase TiO_2 (JCPDS card file: 21-1272). Trace amounts of rutile TiO_2 present in
242 $\text{Fe}_2\text{O}_3\text{-TiO}_2$ were represented at 27.4 , 36.0 , 39.2 , 54.2 , 56.7 , 69.9°, which were assigned to
243 (110), (101), (200), (211), (220), and (112) planes, respectively (JCPDS card file: 21-1276). The

244 presence of both anatase and rutile phases was due to the mix phases of P25 (anatase: ~80% and
245 rutile: ~20%) used as a material to fabricate Fe₂O₃-TiO₂. Meanwhile, traces of Fe₂O₃ present in
246 Fe₂O₃-TiO₂ showed lower peak intensities at 30.2, 35.5, 57.0, and 62.9°, which were indexed to
247 (220), (311), (511), and (440) planes, respectively (JCPDS card file: 39-1346). The low peak
248 intensities were due to low concentration of Fe₂O₃ (1 mol%) added during the fabrication of
249 Fe₂O₃-TiO₂ [12]. Upon closer observation, angular positions of certain XRD peaks of the
250 synthesized Fe₂O₃-TiO₂ were slightly shifted as compared to the peaks of P25. This implied a
251 small distortion in TiO₂ crystal lattice due to presence of Fe. The TiO₂ lattice distortion was a
252 result from Ti⁴⁺ replaced by Fe³⁺ because of their comparable radii (0.068 and 0.064 nm,
253 respectively) [8,35]. A substitution of Ti⁴⁺ by Fe³⁺ increased the number of oxygen vacancies,
254 which promoted photoactivity of Fe₂O₃-TiO₂ [35]. Overall, the XRD patterns of Fe₂O₃-TiO₂
255 established the coexistence of Fe₂O₃, anatase and rutile TiO₂ crystalline structures. Additionally,
256 average crystallite sizes of Fe₂O₃-TiO₂, P25, and Fe₂O₃ were 22.99, 24.29, and 17.45 nm,
257 respectively (Table 1).

258

259 3.1.3. Effect of Fe₂O₃ loading

260 PL measurement was conducted to evaluate the correlation between photoactivity of Fe₂O₃-
261 TiO₂ and Fe₂O₃ loading. Peak intensity of PL spectra correlated to the recombination rate of
262 electron-hole pairs whereby weaker peak intensity represented lower recombination rate [36].
263 According to the PL signals (Fig. 6), an addition of Fe₂O₃ from 0.4 to 1.2 mol% reduced the PL
264 peak intensities, signifying better charge separation at higher Fe₂O₃ molar content. Due to the
265 close radii of Fe³⁺ (0.064 nm) and Ti⁴⁺ (0.068 nm), an increase of Fe₂O₃ loading led to more
266 substitution of Ti⁴⁺ by Fe³⁺, consequently, generating more oxygen vacancies [35]. An increase

267 in oxygen vacancies, which acted as electron donors in TiO₂ lattice, promoted better charge
268 separation. On the other hand, excessive addition of Fe₂O₃ could cause an undesirable energy
269 transfer between nearby ions due to shorter distance of Fe-Fe ions, leading to a deterioration in
270 charge separation and reduction in photoactivity [35]. As a comparison, the synthesized Fe₂O₃-
271 TiO₂ exhibited a significant 84% reduction in PL emission intensity as compared to P25 (Fig. 6).
272 The reduction of emission intensity signified a high efficiency of charge separation and transfer
273 between the two Fe₂O₃ and TiO₂ metal oxides in the synthesized Fe₂O₃-TiO₂ [37]. Theoretically,
274 an incorporation of Fe₂O₃ into TiO₂ lattice resulted in the substitution of Ti⁴⁺ by Fe³⁺ species,
275 creating oxygen vacancies, which in turn supported charge separation [35].

276 Band gap measurements from diffuse reflectance study pave way to a better understanding
277 of the optical response of fabricated Fe₂O₃-TiO₂ [38]. Band gaps of Fe₂O₃-TiO₂ samples at
278 different Fe₂O₃ loading are displayed in the transformed Kubelka-Munk function plot (Fig. 7a).
279 Although the band gap values were in close range (2.85-2.95 eV) despite a change in Fe₂O₃
280 molar content, the photodegradation efficiency (Fig. 8) improved significantly from 40.6 to
281 62.5% with increasing Fe₂O₃ loading (0.4 to 1.2 mol%, respectively). Upon light absorption,
282 excited electrons from TiO₂ conduction band were transferred to the interface of Fe₂O₃ and
283 converted Fe³⁺ into Fe²⁺ [37,39]. Since the unstable Fe²⁺ was rapidly oxidized by dissolved
284 oxygen to Fe³⁺, Fe³⁺ once again behaved as a shallow trapping site for photoexcited electrons
285 from TiO₂, hindering electron-hole pair recombination [36,39]. So, at higher Fe₂O₃ molar
286 content, more Fe³⁺ was incorporated into TiO₂ lattice [40]. Thus, electron-hole recombination
287 was suppressed more effectively and enhanced the photoactivity of Fe₂O₃-TiO₂ [40]. However,
288 further addition of Fe₂O₃ beyond 1.0 mol% did not help to improve photoactivity of the catalyst
289 due to high percentage of free Fe₂O₃ (Fe³⁺), which was not incorporated into TiO₂ lattice [40].

290 On the other hand, band gap values of $\text{Fe}_2\text{O}_3\text{-TiO}_2$ were enhanced considerably as compared to
291 P25 (Table 1 and Fig. 7a). An improvement in band gap values indicated a successful
292 incorporation of Fe^{3+} into the TiO_2 framework [40]. Notably, coupling of Fe_2O_3 with TiO_2
293 stimulated better light harvesting ability and further extended the light absorption range as shown
294 in Fig. 7b. In addition, plot of transformed Kubelka-Munk function (Fig. 7a) reveals that band
295 gap energy of $\text{Fe}_2\text{O}_3\text{-TiO}_2$ was lower (2.95 eV) than P25 (3.35 eV). This observation was
296 probably due to electronic coupling between the wide band gap of TiO_2 with the narrow band
297 gap of Fe_2O_3 [41].

298 Based on one-way ANOVA, maximum photodegradation efficiency of PPME (62.3% COD
299 removal) was observed at 20 min of milling time, 250 rpm of milling speed, and 1 mol% of
300 Fe_2O_3 loading. The synthesized $\text{Fe}_2\text{O}_3\text{-TiO}_2$ photocatalyst was 1.5-times more superior to the
301 commercial P25 (40.6% COD removal).

302

303 **3.2. Comparison of other metal oxide- TiO_2 photocatalysts with $\text{Fe}_2\text{O}_3\text{-TiO}_2$**

304

305 Other metal oxide candidates (WO_3 , ZnO , and CeO_2) were introduced into the TiO_2 lattice
306 under recommended milling conditions and their photocatalytic activity was compared with
307 $\text{Fe}_2\text{O}_3\text{-TiO}_2$. Based on the photodegradation of PPME (Fig. 9 and Table 4), it was apparent that
308 $\text{Fe}_2\text{O}_3\text{-TiO}_2$ attained the highest COD removal (62.3%) as compared to other metal oxide- TiO_2
309 photocatalysts (35.4-45.5%), P25 (40.6%), anatase TiO_2 (24.9%), rutile TiO_2 (2.9%), and Fe_2O_3
310 (1.1%). Therefore, $\text{Fe}_2\text{O}_3\text{-TiO}_2$ was established as a desired and promising photocatalyst to
311 degrade PPME in this work.

312

313 **3.3. Detailed characterizations of Fe₂O₃-TiO₂**

314

315 The fabricated Fe₂O₃-TiO₂ under recommended milling conditions (20 min of milling time,
316 250 rpm of milling speed, and 1 mol% of Fe₂O₃ loading) was subjected to additional
317 characterization studies to further investigate its catalytic properties.

318

319 **3.3.1. Elemental compositions and distribution**

320 EDX spectrum (Fig. 10a) shows simultaneous presence of Fe, Ti and O elements in Fe₂O₃-
321 TiO₂, which was produced through mechanochemical process. In addition, EDX mapping (Fig.
322 10b-d) shows extensive dispersion of Fe and O elements within the TiO₂ framework. This result
323 indicated that Fe₂O₃ was well distributed throughout the fabricated Fe₂O₃-TiO₂ using
324 mechanochemical process. Elemental compositions of Fe₂O₃-TiO₂ sample was further verified
325 using XPS analysis.

326 In order to ascertain the chemical states of Fe, Ti and O existing in Fe₂O₃-TiO₂, XPS
327 analysis was conducted. As displayed in Fig. 11a, XPS survey spectrum detected the presence of
328 Fe (Fe 2p), Ti (Ti 2p), and O (O 1s) in Fe₂O₃-TiO₂. Carbon peak (C 1s) was attributed to the
329 carbon tape used as a support during XPS analysis. High resolution XPS spectra reveal chemical
330 species within the prepared Fe₂O₃-TiO₂ (Fig. 11b-d). Binding energies of Fe 2p_{3/2} and Fe 2p_{1/2}
331 were 710.7 and 724.5 eV respectively, verifying the presence of Fe³⁺. An absence of peaks
332 around 707 and 719 eV ruled out the presence of Fe²⁺, firmly supporting the addition of γ -Fe₂O₃
333 phase into TiO₂ [42]. Peaks corresponding to Ti⁴⁺ were centered at 458.6 and 464.4 eV, which
334 were analogous to Ti 2p_{3/2} and Ti 2p_{1/2}, respectively. From O 1s spectra, binding energy at 529.8

335 eV was assigned to lattice oxygen, O^{2-} species from Fe_2O_3 and Ti-O-Ti [34,43]. The attained XPS
336 findings (Fig. 11a-d) were in conformity with the obtained EDX analysis data (Fig. 10a).

337

338 **3.3.2. Surface morphology**

339 TEM image (Fig. 12a) shows that Fe_2O_3 - TiO_2 nanoparticles had an average particle size of
340 30 nm. Darker regions corresponded to Fe_2O_3 particles whereas lighter regions were ascribed to
341 TiO_2 nanoparticles. Noticeably, an intimate contact between Fe_2O_3 and TiO_2 particles was
342 formed from mechanochemical process. The contact was advantageous for charge transfer
343 between the two metal oxides due to a shorter carrier diffusion length that would suppress
344 recombination of electron-hole pairs [37]. Furthermore, Fe_2O_3 particles appeared to be well-
345 dispersed throughout the Fe_2O_3 - TiO_2 sample. High resolution TEM (HRTEM) image (Fig. 12b)
346 revealed clear lattice fringes of Fe_2O_3 and TiO_2 . Lattice fringe of 0.29 nm was equivalent to
347 (220) plane of γ - Fe_2O_3 , whereas lattice fringes of 0.35 and 0.32 nm corresponded to (101)
348 anatase plane and (110) rutile plane of TiO_2 , respectively [43,44].

349

350 **3.3.3. Raman analysis**

351 Based on Raman spectrum of the Fe_2O_3 - TiO_2 sample (Fig. 13), major Raman peaks at 155,
352 394, 514, and 633 cm^{-1} were indexed to the typical structure of TiO_2 whereas peak at 205 cm^{-1}
353 indicated the presence of γ - Fe_2O_3 [35,45]. A formation of Fe-O-Ti bond in the fabricated Fe_2O_3 -
354 TiO_2 was evidenced by a peak at 279 cm^{-1} . This denoted that Fe^{3+} replaced some Ti^{4+} species in
355 lattice sites of the crystalline structure, indicating a successful synthesis of Fe_2O_3 - TiO_2
356 photocatalyst [35]. Peak intensity analogous to the presence of Fe_2O_3 was low due to low
357 concentration of Fe_2O_3 (1 mol%). An incorporation of Fe atoms into Ti lattice sites also caused a

358 shift of peaks to slightly greater frequencies as a result from force constant and vibrational
359 amplitudes of neighbouring bonds [34,35].

360

361 **3.3.4. FTIR analysis**

362 FTIR analysis was employed to determine the functional groups present in Fe₂O₃-TiO₂ [21].
363 Based on Fig. 14, FTIR spectrum of Fe₂O₃-TiO₂ was similar to P25, signifying that Fe₂O₃ was
364 well-infused into the TiO₂ lattice [39]. Two bands observed at 3400 and 1634 cm⁻¹ were
365 characteristics of O-H stretching vibrations and H-OH bending of hydroxyl groups present [46].
366 These bands played a significant role in photocatalytic reactions to react with photogenerated
367 holes on the Fe₂O₃-TiO₂ surface upon light irradiation. Broad peak at 3250 cm⁻¹ was due to O-H
368 stretching vibration of water whereas bands at 2924 and 2840 cm⁻¹ were attributed to C-H
369 stretching vibrations of alkyl chain [40,42].

370

371

372 **4. Conclusions**

373

374 In this study, a photoactive Fe₂O₃-TiO₂ catalyst was successfully synthesized using a one-
375 step facile and solvent-free mechanochemical process under ambient temperature and
376 atmospheric pressure. Characterization studies showed that the synthesized Fe₂O₃-TiO₂
377 possessed crystalline structures of γ -Fe₂O₃, anatase, and rutile phases of TiO₂. It was further
378 confirmed that Fe, Ti and O elements were present and were well-dispersed within the Fe₂O₃-
379 TiO₂ framework. Enhanced photoactivity of Fe₂O₃-TiO₂ was attributed to the following
380 distinctive traits: (i) formation of Fe-O-Ti bond due to substitution of Ti⁴⁺ by Fe³⁺ in TiO₂ lattice;

381 (ii) higher specific surface area ($58.40 \text{ m}^2/\text{g}$) and porosity ($0.29 \text{ cm}^3/\text{g}$) than commercial P25; (iii)
382 lower band gap (2.95 eV) than P25 due to electronic coupling of TiO_2 and Fe_2O_3 ; (iv) and
383 suppressed electron-hole recombination rate, which was ascribed to the incorporation of Fe^{3+} that
384 acted as a charge-transfer mediator. In addition, the highest treatment efficiency of PPME
385 (62.3% of COD removal) was achieved by using $\text{Fe}_2\text{O}_3\text{-TiO}_2$, which was synthesized at 20 min
386 of milling time, 250 rpm of milling speed, and 1 mol% of Fe_2O_3 loading. Markedly, the
387 photoactivity of $\text{Fe}_2\text{O}_3\text{-TiO}_2$ was 53.4% higher than the commercial P25. In conclusion, this
388 study provided a better insight into the potential use of mechanochemical process as a greener,
389 simpler and low-cost approach in synthesizing high efficiency photocatalysts to degrade complex
390 industrial effluent.

391

392 **Acknowledgements**

393 The authors would like to thank Monash University Malaysia for providing W. Subramonian
394 with a Ph.D. scholarship.

395

396 **References**

- 397 [1] C.Y. Teh, P.M. Budiman, K.P.Y. Shak, T.Y. Wu, Recent advancement of coagulation-
398 flocculation and its application in wastewater treatment, *Ind. Eng. Chem. Res.* 55 (2016)
399 4363-4389.
- 400 [2] L. Fernandes, M.S. Lucas, M.I. Maldonado, I. Oller, A. Sampaio, Treatment of pulp mill
401 wastewater by *Cryptococcus podzolicus* and solar photo-Fenton: a case study, *Chem. Eng. J.*
402 245 (2014) 158-165.
- 403 [3] W. Subramonian, T.Y. Wu, Effect of enhancers and inhibitors on photocatalytic sunlight
404 treatment of methylene blue, *Water Air Soil Pollut.* 225 (2014) 1-15.
- 405 [4] C. Lopez-Lopez, J. Martín-Pascual, M.V. Martínez-Toledo, M. M. Muñío, E. Hontoria,
406 J.M. Poyatos, Kinetic modeling of TOC removal by H₂O₂/UV, photo-Fenton and
407 heterogeneous photocatalysis processes, *Int. J. Environ. Sci. Technol.* 12 (2016) 3255-3262.
- 408 [5] H.N. Chin, Z.Z. Noor, N.S.A. Mutamin, K.L. Chi, Green Technology in wastewater
409 treatment technologies: integration of membrane bioreactor with various wastewater
410 treatment systems, *Chem. Eng. J.* 283 (2016) 582-594.
- 411 [6] E. Ghasemi, H. Ziyadi, A.M. Afshar, M. Sillanpää, Iron oxide nanofibers: a new magnetic
412 catalyst for azo dyes degradation in aqueous solution, *Chem.*
413 *Eng. J.* 264 (2015) 146-151.
- 414 [7] D. Wodka, R.P. Socha, E. Bielańska, M. Elźbieciak-Wodka, P. Nowak, P. Warszyński,
415 Photocatalytic activity of titanium dioxide modified by Fe₂O₃ nanoparticles, *Appl. Surf. Sci.*
416 319 (2014) 173-180.
- 417 [8] J.O. Carneiro, S. Azevedo, F. Fernandes, E. Freitas, M. Pereira, C.J. Tavares, S. Lanceros-
418 Méndez, V. Teixeira, Synthesis of iron-doped TiO₂ nanoparticles by ball-milling process:

- 419 the influence of process parameters on the structural, optical, magnetic, and photocatalytic
420 properties, *J. Mater. Sci.* 49 (2014) 7476-7488.
- 421 [9] Y. Su, Z. Wu, Y. Wu, J. Yu, L. Sun, C. Lin, Acid orange II degradation through a
422 heterogeneous Fenton-like reaction using Fe-TiO₂ nanotube arrays as a photocatalyst, *J.*
423 *Mater. Chem. A.* 3 (2015) 8537-8544.
- 424 [10] F.C.F. Low, T.Y. Wu, C.Y. Teh, J.C. Juan, N. Balasubramanian, Investigation into
425 photocatalytic decolorisation of CI Reactive Black 5 using titanium dioxide nanopowder,
426 *Color. Technol.* 128 (2012) 44-50.
- 427 [11] D. Liū, Z. Li, W. Wang, G. Wang, D. Liú, Hematite doped magnetic TiO₂ nanocomposites
428 with improved photocatalytic activity, *J. Alloy. Compd.* 654 (2016) 491-497.
- 429 [12] S. Neubert, D. Mitoraj, S.A. Shevlin, P. Pulisova, M. Heimann, Y. Du, G.K.L. Goh, M.
430 Pacia, K. Kruczata, S. Turner, W. Macyk, Z.X. Guo, R.K. Hocking, R. Beranek, Highly
431 efficient rutile TiO₂ photocatalysts with single Cu(II) and Fe(III) surface catalytic sites, *J.*
432 *Mater. Chem. A.* 4 (2016) 3127-3138.
- 433 [13] A. Luengnaruemitchai, K. Srihamat, C. Pojanavaraphan, R. Wanchanthuek, Activity of
434 Au/Fe₂O₃-TiO₂ catalyst for preferential CO oxidation, *Int. J. Hydrog. Energy* 40 (2015)
435 13443-13455.
- 436 [14] S. Zhang, Q. Zhong, Y. Shen, L. Zhu, J. Ding, New insight into the promoting role of
437 process on the CeO₂-WO₃/TiO₂ catalyst for NO reduction with NH₃ at low-temperature, *J.*
438 *Colloid Interface Sci.* 448 (2015) 417-426.
- 439 [15] M. Naimi-Joubani, M. Shirzad-Siboni, J.-K. Yang, M. Gholami, M. Farzadkia,
440 Photocatalytic reduction of hexavalent chromium with illuminated ZnO/TiO₂ composite, *J.*
441 *Ind. Eng. Chem.* 22 (2015) 317-323.

- 442 [16] K.-R. Wee, B.D. Sherman, M.K. Brennaman, M.V. Sherridan, A. Nayak, L. Alibabaei, T.J.
443 Meyer, An aqueous, organic dye derivated $\text{SnO}_2/\text{TiO}_2$ core/shell photoanode, *J. Mater.*
444 *Chem. A* 4 (2016) 2969-2975.
- 445 [17] W. Deng, Q. Dai, Y. Lao, B. Shi, X. Wang, Low temperature catalytic combustion of 1,2-
446 dichlorobenzene over $\text{CeO}_2\text{-TiO}_2$ mixed oxide catalysts, *Appl. Catal. B-Environ.* 181 (2016)
447 848-861.
- 448 [18] S. Fathinia, M. Fathinia, A.A. Rahmani, A. Khataee, Preparation of natural pyrite
449 nanoparticles by high energy planetary ball milling as a nanocatalyst for heterogeneous
450 Fenton process, *Appl. Surf. Sci.* 327 (2015) 190-200.
- 451 [19] C.Y. Teh, T.Y. Wu, J.C. Juan, Facile sonochemical synthesis of N,Cl-codoped TiO_2 :
452 synthesis effects, mechanism and photocatalytic performance, *Catal. Today* 256 (2015) 365-
453 374.
- 454 [20] K. Wieczorek-Ciurowa, K. Gamrat, Mechanochemical synthesis as an example of green
455 processes, *J. Therm. Anal. Calorim.* 88 (2007) 213-217.
- 456 [21] Ž. Kesić, I. Lukić, M. Zdujić, Č. Jovalekić, H. Liu, D. Skala, Mechanochemical synthesis of
457 $\text{CaO}\cdot\text{ZnO}\cdot\text{K}_2\text{CO}_3$ catalyst: characterization and activity for methanolysis of sunflower oil,
458 *Chem. Ind. Chem. Eng.* 21 (2015) 1-12.
- 459 [22] S. Lu, J. Huang, Z. Peng, X., Li, J. Yan, Ball-milling 2,4,6-trichlorophenol with calcium
460 oxide: dechlorination experiment and mechanism considerations, *Chem. Eng. J.* 195-196
461 (2012) 62-68.
- 462 [23] K. Ralphs, C. Hardacre, S.L. James, Application of heterogeneous catalyst prepared by
463 mechanochemical synthesis, *Chem. Soc. Rev.* 42 (2013) 7701-7718.

- 464 [24] A. Banerjee, R. Gupta, K. Balani, Non-monotonic lattice parameter variation in ball-milled
465 ceria, *J. Mater. Sci.* 50 (2015) 6349-6358.
- 466 [25] C. Xu, S. De, A.M. Balu, M. Ojeda, R. Luque, Mechanochemical synthesis of advanced
467 nanomaterials for catalytic applications, *Chem. Commun.* 15 (2015) 6698-6713.
- 468 [26] T.J. Clarke, T.E. Davies, S.A. Kondrat, S.H. Taylor, Mechanochemical synthesis of copper
469 manganese oxide for the ambient temperature oxidation of carbon monoxide, *Appl. Catal.*
470 *B-Environ.* 165 (2015) 222-231.
- 471 [27] W. Subramonian, T.Y. Wu, S.-P. Chai, A comprehensive study on coagulant performance
472 and floc characterization of natural *Cassia obtusifolia* seed gum in treatment of raw pulp and
473 paper mill effluent, *Ind. Crops Prod.* 61 (2014) 317-324.
- 474 [28] W. Subramonian, T.Y. Wu, S.-P. Chai, An application of response surface methodology for
475 optimizing coagulation process of raw industrial effluent using *Cassia obtusifolia* seed gum
476 together with alum, *Ind. Crops Prod.* 70 (2015) 107-115.
- 477 [29] S.D. House, J.J. Vajo, C. Ren, A.A. Rockett, I.M. Robertson, Effect of ball milling duration
478 and dehydrogenation on the morphology, microstructure and catalyst dispersion in Ni-
479 catalyzed MgH₂ hydrogen storage materials, *Acta Mater.* 86 (2015) 55-68.
- 480 [30] X. Chen, T. Lu, Z. Lu, L. Chen, Q. Zhang, G. Cheng, J. Qi, Systematic optimization of ball-
481 milling for highly transparent Yb:YAG ceramic using co-precipitated raw powders, *J. Alloy.*
482 *Compd.* 653 (2015) 552-560.
- 483 [31] Y.H. Taufiq-Yap, C.K. Goh, G.J. Hutchings, N. Dummer, J.K. Bartley, Effects of
484 mechanochemical treatment to the vanadium phosphate catalysts derived from
485 VOPO₄·2H₂O, *J. Mol. Catal. A-Chem.* 260 (2006) 24-31.

- 486 [32] F.M.T. Mendes, A.C.C. Marques, D.L. Mendonça, M.S. Oliveira, R.O. Moutta, V.S.
487 Ferreira-Leitão, High surface area activated carbon from sugar cane straw, *Waste Biomass*
488 *Valor.* 6 (2015) 433-440.
- 489 [33] N. Aman, N.N. Das, T. Mishra, Effect of N-doping on visible light activity of TiO₂-SiO₂
490 mixed oxide photocatalysts, *J. Environ. Chem. Eng.* 4 (2016) 191-196.
- 491 [34] L. Qin, X. Pan, L. Wang, X. Sun, G. Zhang, X. Guo, Facile preparation of mesoporous TiO₂
492 (B) nanowires with well-dispersed Fe₂O₃ nanoparticles and their photochemical catalytic
493 behavior, *Appl. Catal. B-Environ.* 150-151 (2014) 544-553.
- 494 [35] A. Banisharif, A.A. Khodadadi, Y. Mortszavi, A.A. Firooz, J. Behestian, S. Agah, S.
495 Menbari, Highly active Fe₂O₃-doped TiO₂ photocatalyst for degradation of trichloroethylene
496 in air under UV and visible light irradiation: experimental and computational studies, *Appl.*
497 *Catal. B-Environ.* 165 (2015) 209-221.
- 498 [36] W. Li, X. Liu, H. Li, Hydrothermal synthesis of graphene/Fe³⁺-doped TiO₂ nanowire
499 composites with highly enhanced photocatalytic activity under visible light irradiation, *J.*
500 *Mater. Chem. A* 3 (2015) 15214-15224.
- 501 [37] S.J.A. Moniz, S.A. Shevlin, X. An, Z.-X. Guo, J. Tang, Fe₂O₃-TiO₂ nanocomposites for
502 enhanced charge separation and photocatalytic activity, *Chem. Eur. J.* 20 (2014) 15571-
503 15579.
- 504 [38] G.S. Pozan, M. Isleyen, S. Gokcen, Transition metal coated TiO₂ nanoparticles: synthesis,
505 characterization and their photocatalytic activity, *Appl. Catal. B-Environ.* 140-141 (2013)
506 537-545.

- 507 [39] T.K. Ghorai, M. Chakraborty, P. Pramanik, Photocatalytic performance of nano-
508 photocatalyst from TiO_2 and Fe_2O_3 by mechanochemical synthesis, *J. Alloy. Compd.* 509
509 (2011) 8158-8164.
- 510 [40] B. Palanisamy, C.M. Babu, B. Sundaravel, S. Anandan, V. Murugesan, Sol-gel synthesis of
511 mesoporous mixed $\text{Fe}_2\text{O}_3/\text{TiO}_2$ photocatalyst: application for degradation of 4-chlorophenol,
512 *J. Hazard. Mater.* 252-253 (2013) 233-242.
- 513 [41] Y. Wang, X. Fan, S. Wang, G. Zhang, F. Zhang, Magnetically separable $\gamma\text{-Fe}_2\text{O}_3/\text{TiO}_2$
514 nanotubes for photodegradation of aqueous methyl orange, *Mater. Res. Bull.* 48 (2013) 785-
515 789.
- 516 [42] M.A. Bhosale, D. Ummineni, T. Sasaki, D. Nishio-Hamane, B.M. Bhanage, Magnetically
517 separable $\gamma\text{-Fe}_2\text{O}_3$ nanoparticles: an efficient catalyst for acrylation of alcohols, phenols, and
518 amines using sonication energy under solvent free condition, *J. Mol. Catal. A-Chem.* 404-
519 405 (2015) 8-17.
- 520 [43] G. Wu, Y. Cheng, Y. Ren, Y. Wang, Z. Wang, H. Wu, Synthesis and characterization of $\gamma\text{-Fe}_2\text{O}_3@C$
521 nanorod-carbon sphere composite and its application as microwave absorbing
522 material, *J. Alloy. Compd.* 652 (2015) 346-350.
- 523 [44] P. Mirtchev, K. Liao, E. Jaluague, Q. Qiao, Y. Tian, M. Varela, K.S. Burch, S.J. Pennycook,
524 D.D. Perovic, G. Ozin, $\text{Fe}_2\text{O}_3/\text{Cu}_2\text{O}$ heterostructured nanocrystals, *J. Mater. Chem. A* 2
525 (2014) 8525-8533.
- 526 [45] M.T. Qamar, M. Aslam, I.M.I. Ismail, N. Salah, A. Hameed, The assessment of the
527 photocatalytic activity of magnetically retrievable ZnO coated $\gamma\text{-Fe}_2\text{O}_3$ in sunlight exposure,
528 *Chem. Eng. J.* 283 (2016) 656-667.

- 529 [46] Z.Y. Bai, Q. Yang, J.L. Wang, Fe₃O₄/multi-walled carbon nanotubes as an efficient catalyst
530 for catalyst for catalytic ozonation of p-hydroxybenzoic acid, Int. J. Environ. Sci. Technol.
531 13 (2016) 483-492.

List of Figures

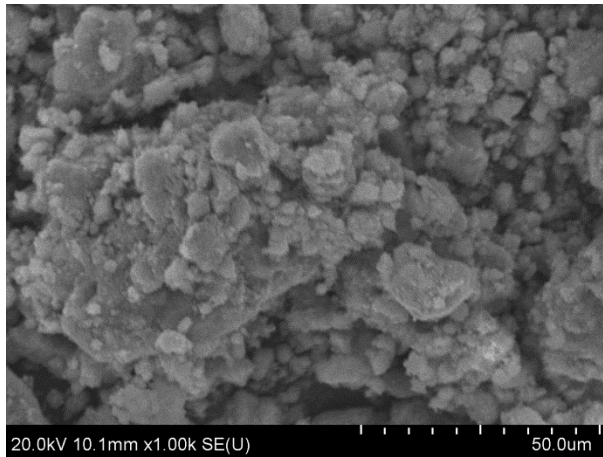


Fig. 1. (a)

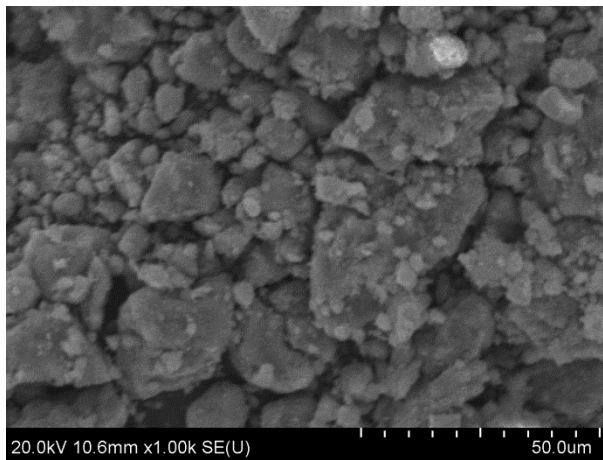


Fig. 1. (b)

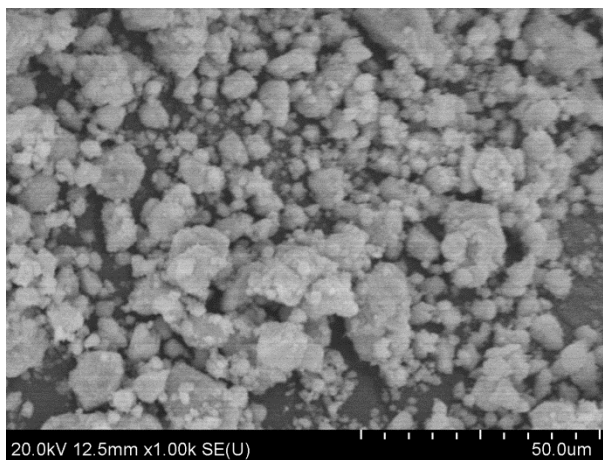


Fig. 1. (c)

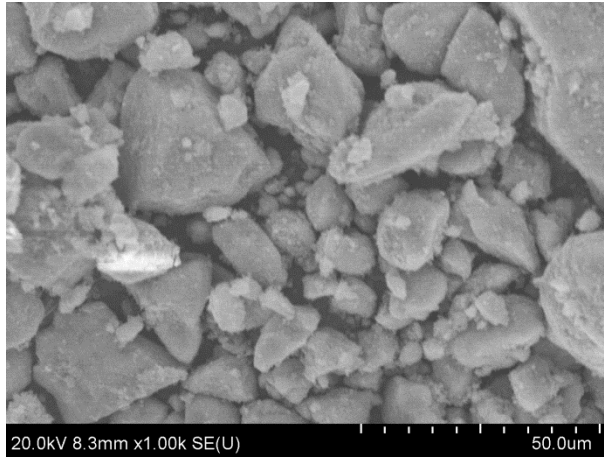


Fig. 1. (d)

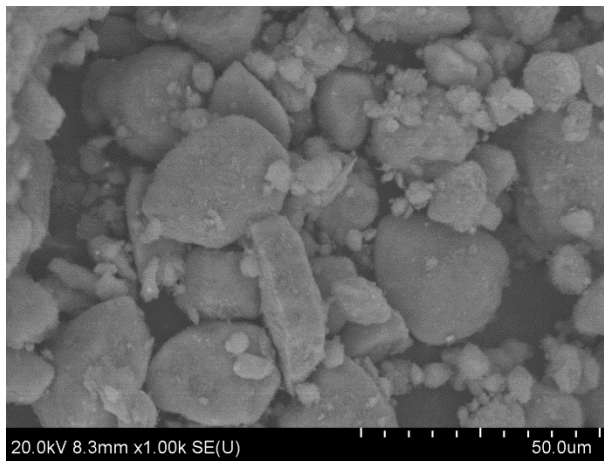


Fig. 1. (e)

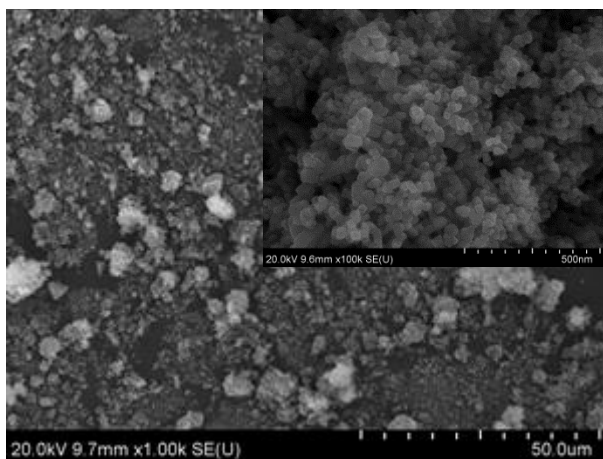


Fig. 1. (f)

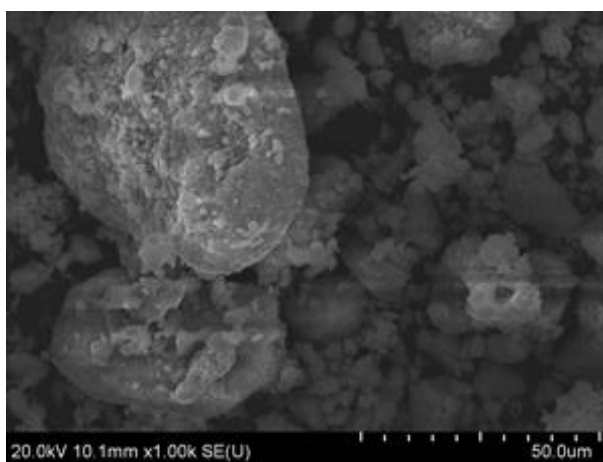


Fig. 1. (g)

Fig. 1. FESEM images of (a) Fe₂O₃-TiO₂ milled at 10 min, (b) 15 min, (c) 20 min, (d) 25 min and (e) 30 min, (f) P25 and (g) Fe₂O₃.

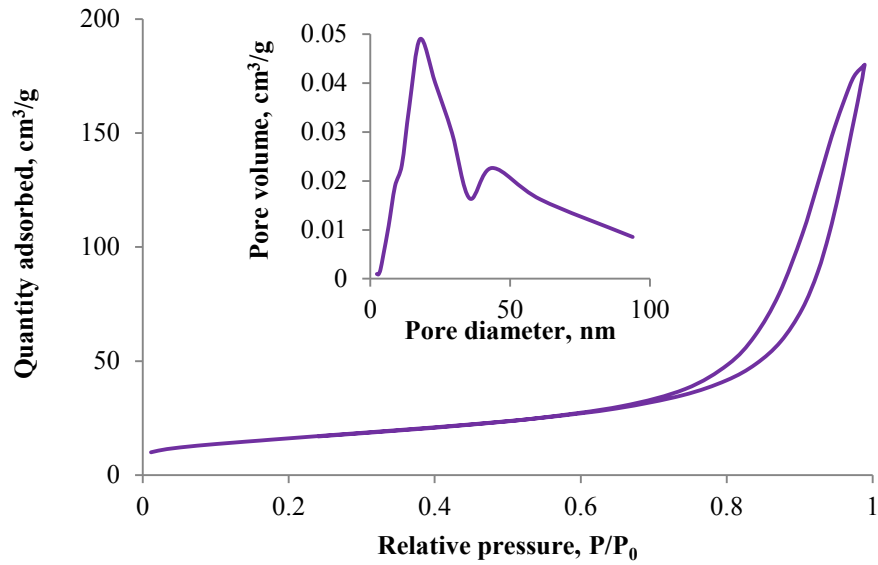


Fig. 2. Nitrogen adsorption/desorption isotherm. Inset shows the BJH pore size distribution of Fe₂O₃-TiO₂.

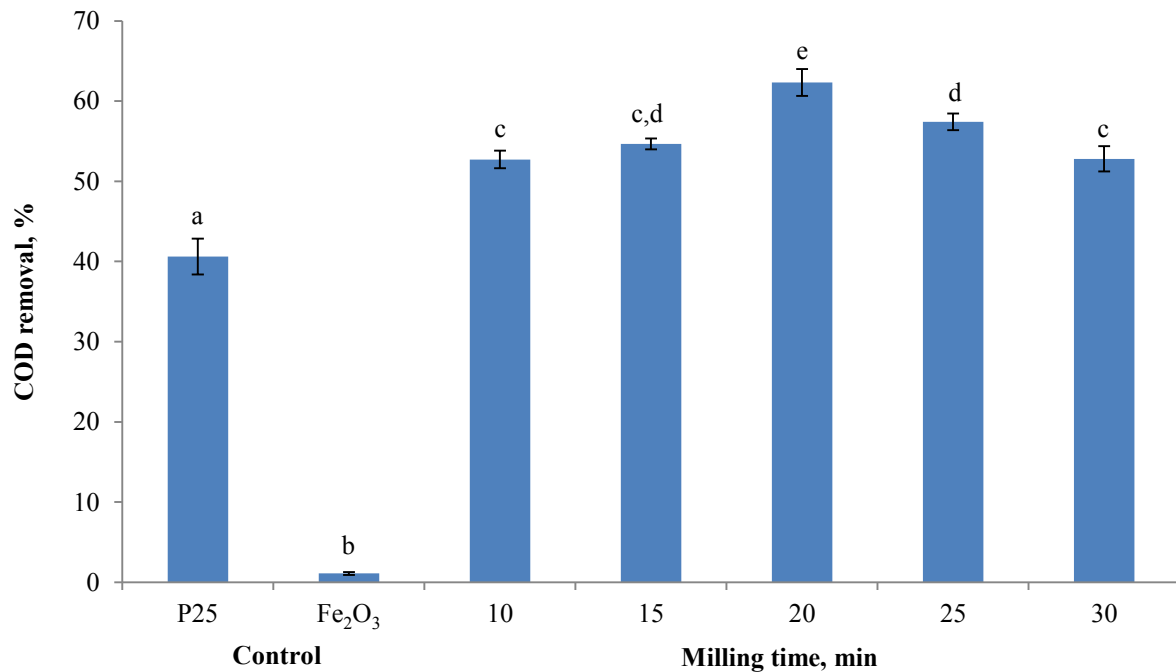


Fig. 3. Effect of milling time on photodegradation of PPME (milling speed = 250 rpm; [Fe₂O₃] = 1 mol%; ball:powder mass ratio = 10:1; irradiation time = 3 h; initial effluent pH = 4; [Fe₂O₃-TiO₂] = 1.0 g/L; air

flow rate = 4.0 L/min; $n = 3$). Values annotated with different letters represent significant differences (one-way ANOVA, Tukey's test; $P < 0.05$).

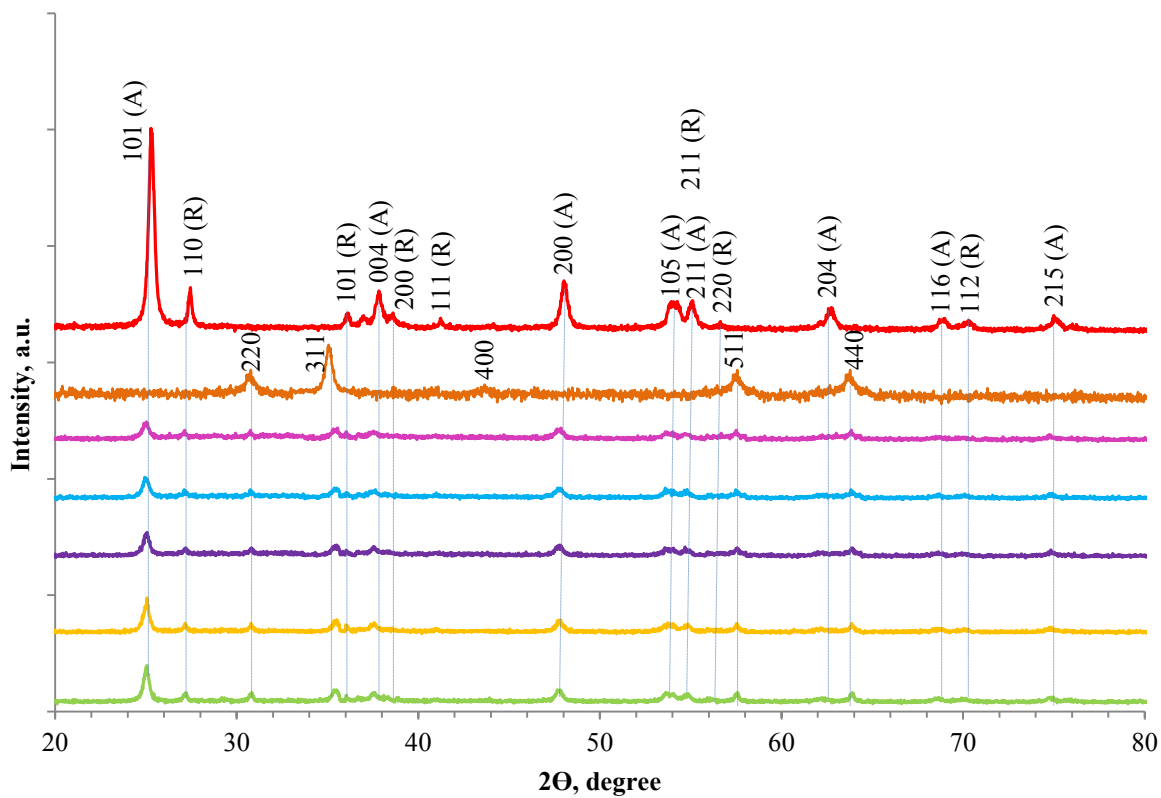


Fig. 4. XRD patterns of P25 (red), Fe_2O_3 (brown), and $\text{Fe}_2\text{O}_3\text{-TiO}_2$ milled at 150 rpm (green), 200 rpm (yellow), 250 rpm (purple), 300 rpm (blue) and 350 rpm (pink) (A: anatase phase; R: rutile phase).

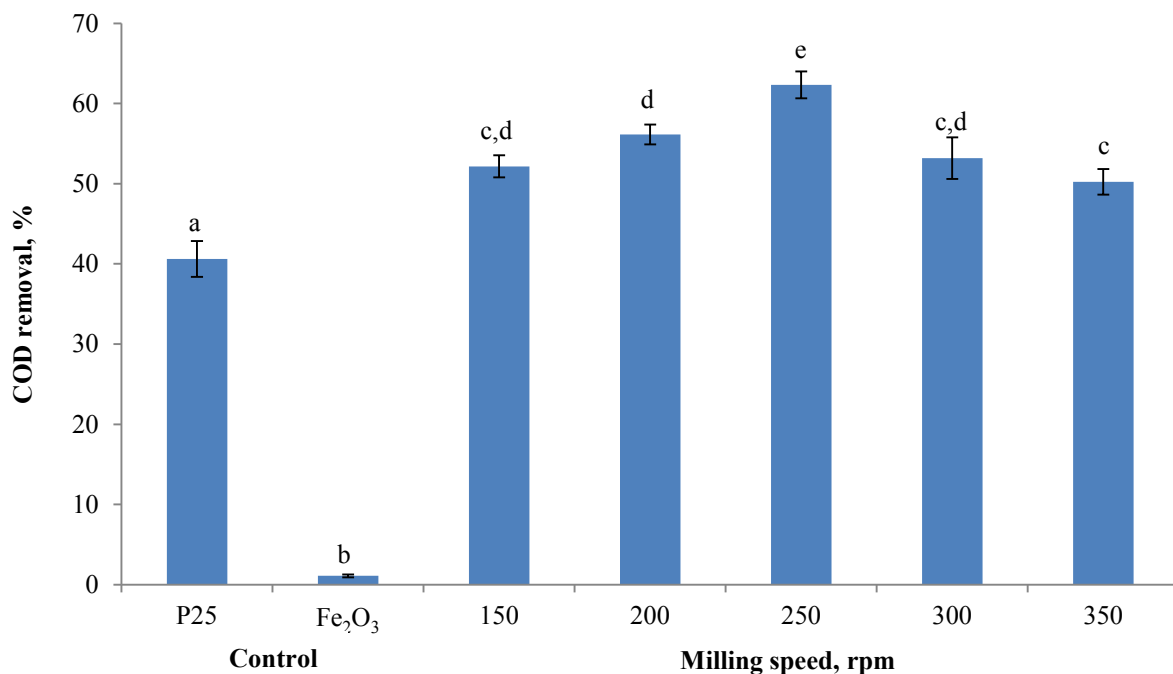


Fig. 5. Effect of milling speed on photodegradation of PPME (milling time = 20 min; [Fe₂O₃] = 1 mol%; ball:powder mass ratio = 10:1; irradiation time = 3 h; initial effluent pH = 4; [Fe₂O₃-TiO₂] = 1.0 g/L; air flow rate = 4.0 L/min; *n* = 3). Values annotated with different letters represent significant differences (one-way ANOVA, Tukey's test; *P* < 0.05).

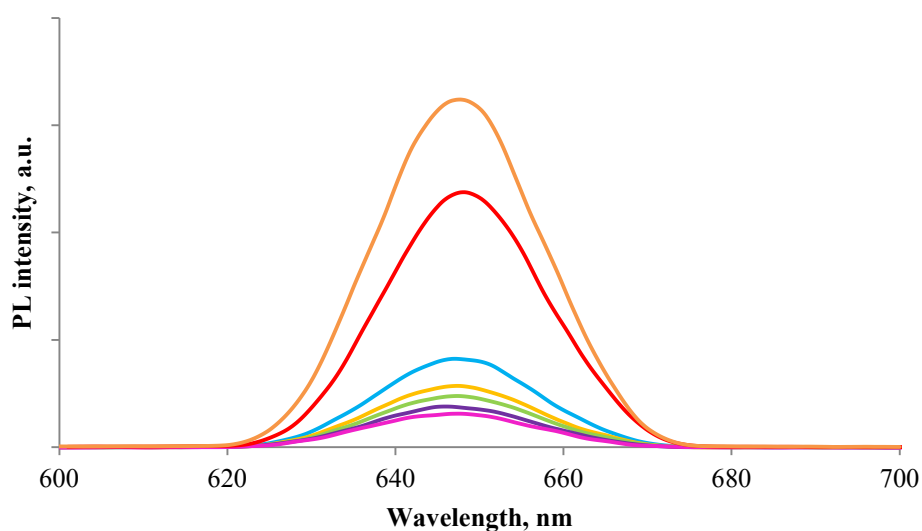


Fig. 6. PL spectra of P25 (red), Fe₂O₃ (brown), and Fe₂O₃-TiO₂ with Fe₂O₃ loading of 0.4 mol% (blue), 0.6 mol% (yellow), 0.8 mol% (green), 1.0 mol% (purple) and 1.2 mol% (pink).

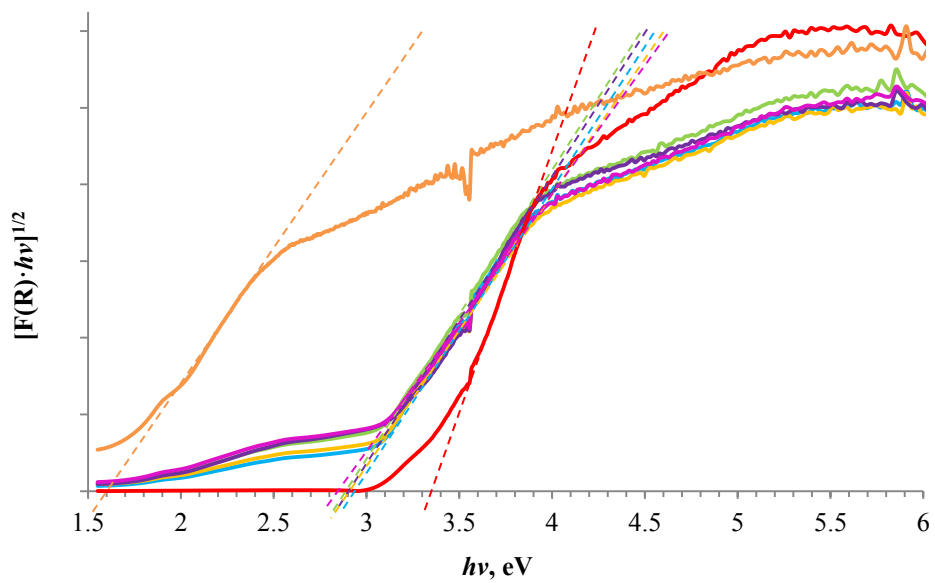


Fig. 7. (a)

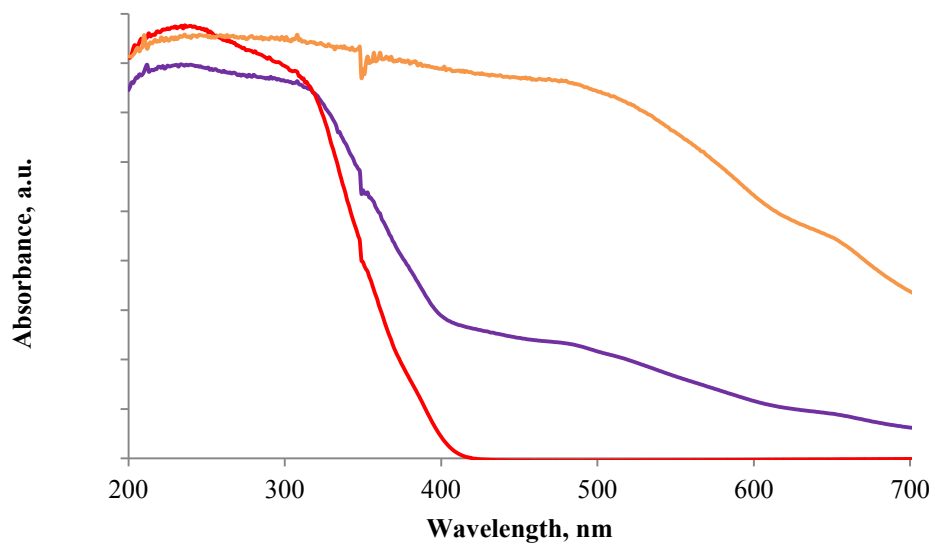


Fig. 7. (b)

Fig. 7. (a) Plot of transformed Kubelka-Munk function $[F(R) \cdot hv]^{1/2}$ versus hv of P25 (red), Fe_2O_3 (brown), and Fe_2O_3 - TiO_2 with Fe_2O_3 loading of 0.4 mol% (blue), 0.6 mol% (yellow), 0.8 mol% (green), 1.0 mol% (purple) and 1.2 mol% (pink). (b) DRS spectra of P25 (red), Fe_2O_3 (brown), and Fe_2O_3 - TiO_2 with Fe_2O_3 loading 1.0 mol% (purple).

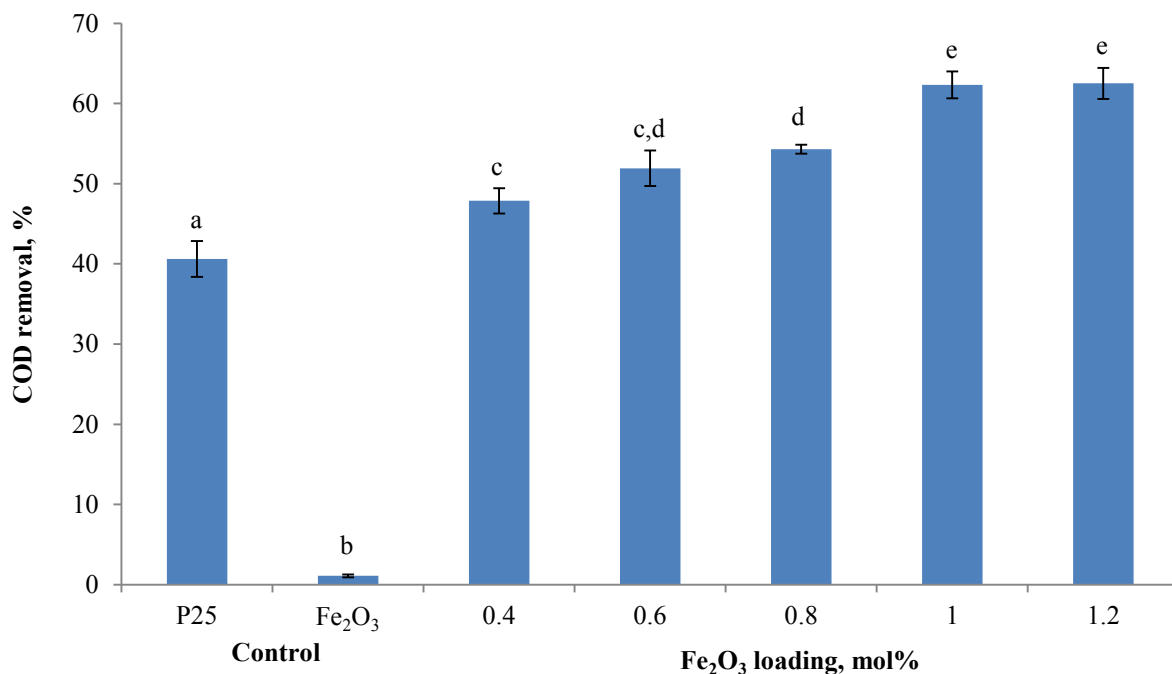


Fig. 8. Effect of Fe₂O₃ loading on photodegradation of PPME (milling time = 20 min; milling speed = 250 rpm; ball:powder mass ratio = 10:1; irradiation time = 3 h; initial effluent pH = 4; [Fe₂O₃-TiO₂] = 1.0 g/L; air flow rate = 4.0 L/min; *n* = 3). Values annotated with different letters represent significant differences (one-way ANOVA, Tukey's test; *P* < 0.05).

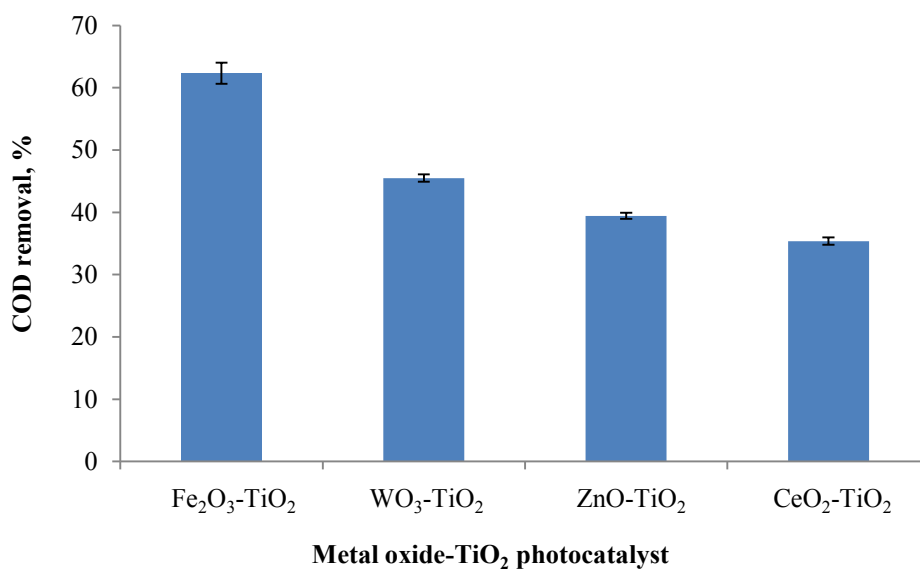


Fig. 9. Comparison of other metal oxide-TiO₂ photocatalysts with Fe₂O₃-TiO₂.

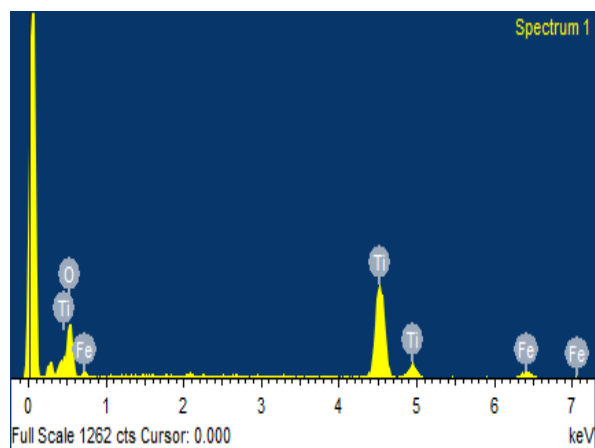


Fig. 10. (a)

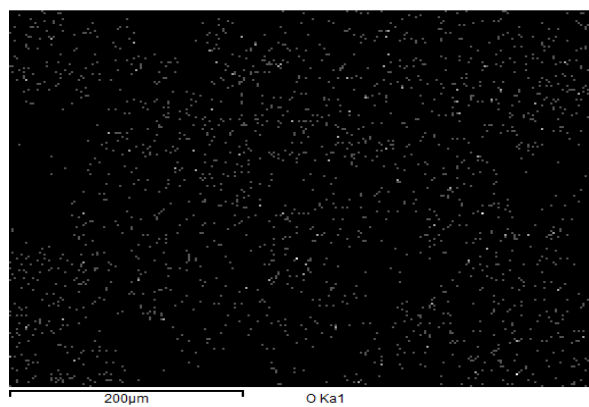


Fig. 10. (b)

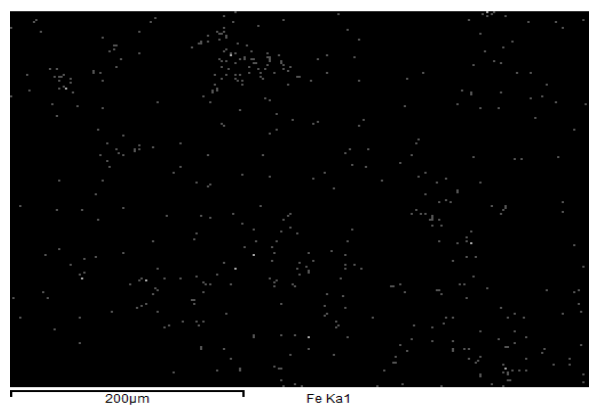


Fig. 10. (c)

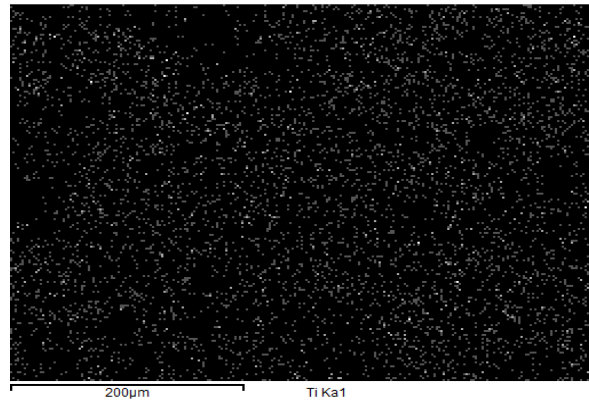


Fig. 10. (d)

Fig. 10. (a) EDX spectrum of $\text{Fe}_2\text{O}_3\text{-TiO}_2$. EDX mapping of (b) O, (c) Fe, and (d) Ti elements in $\text{Fe}_2\text{O}_3\text{-TiO}_2$.

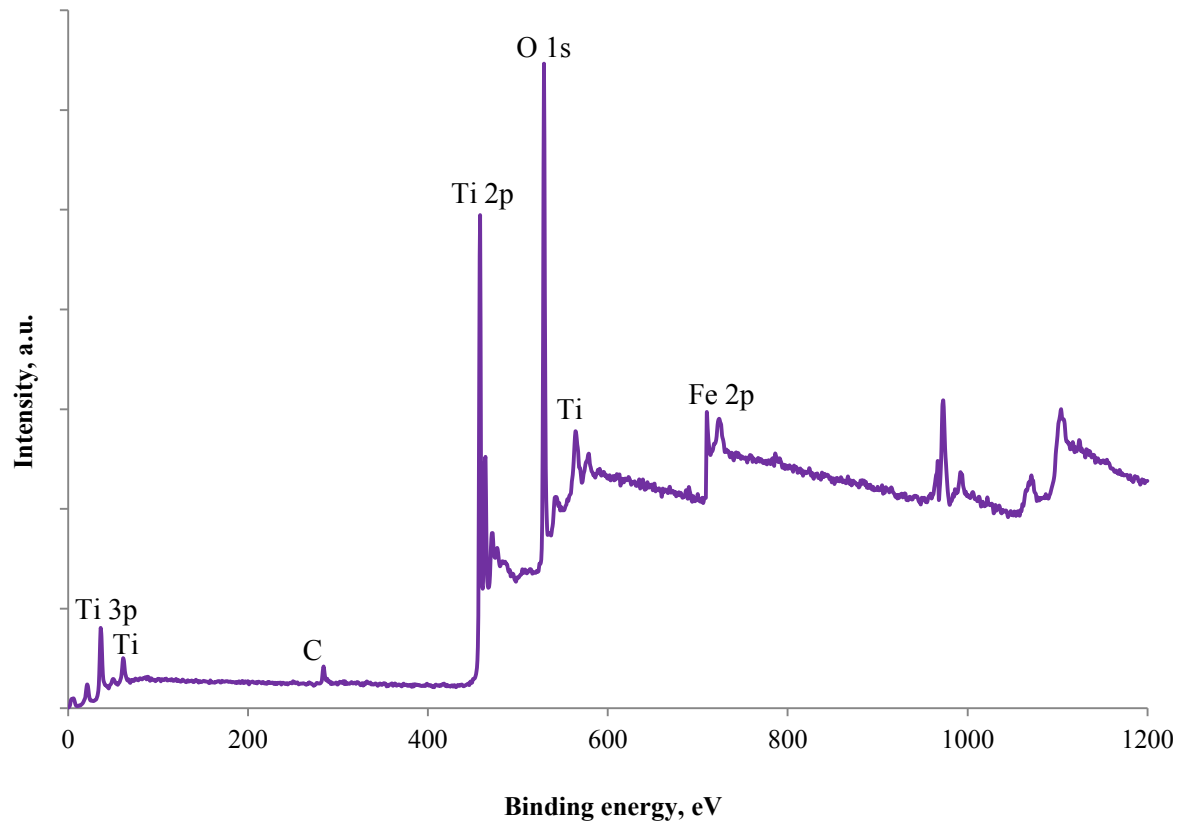


Fig. 11. (a)

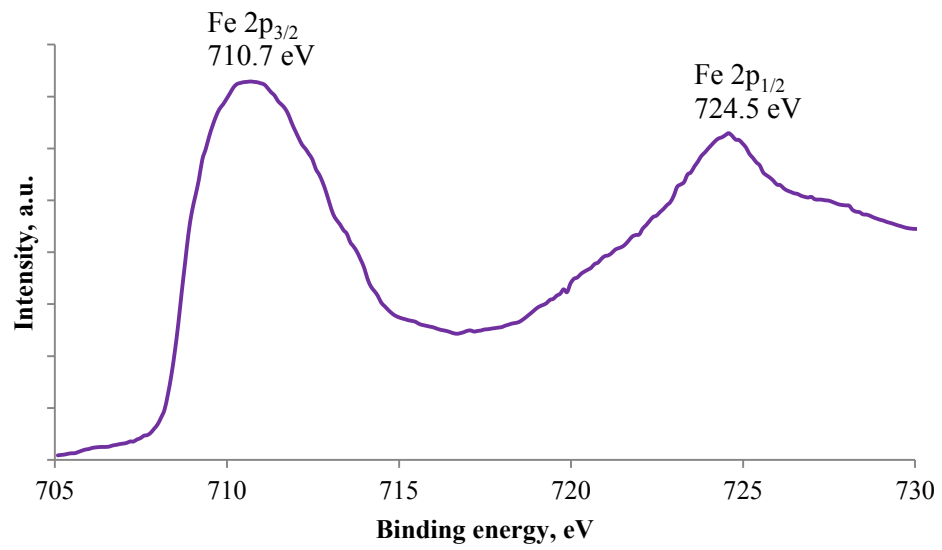


Fig. 11. (b)

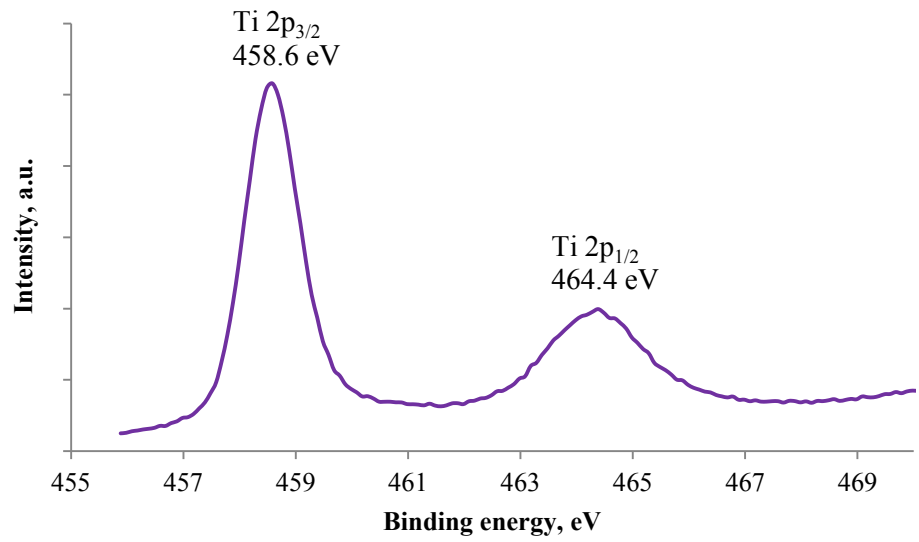


Fig. 11. (c)

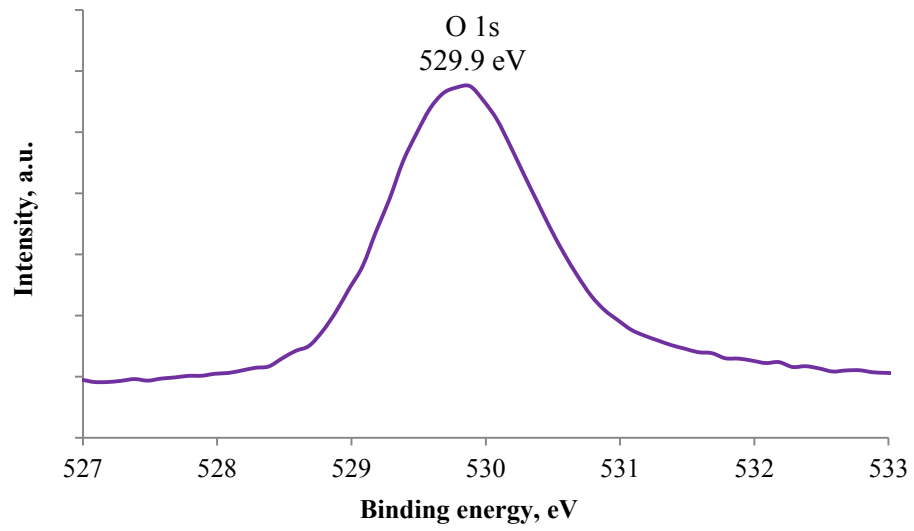


Fig. 11. (d)

Fig. 11. XPS (a) survey spectrum and narrow spectra of (b) Fe 2p, (c) Ti 2p, and (d) O 1s of Fe₂O₃-TiO₂.

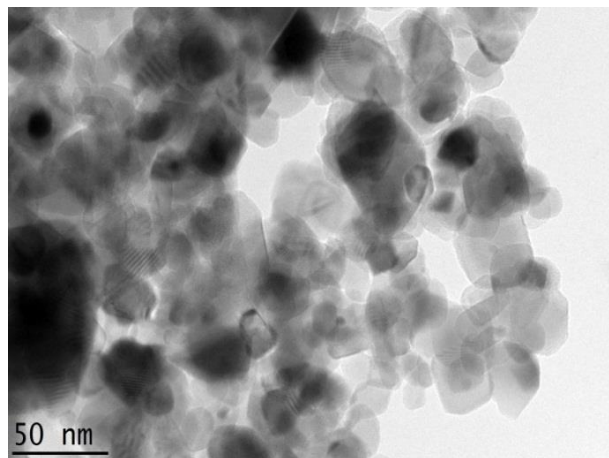


Fig. 12. (a)

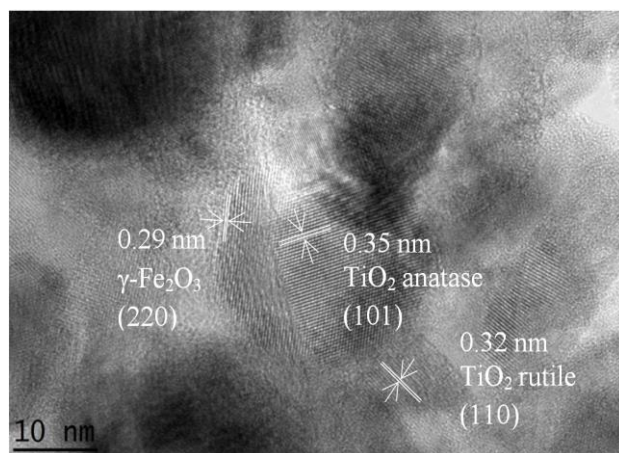


Fig. 12. (b)

Fig. 12. (a) TEM image of Fe₂O₃-TiO₂. **(b)** HRTEM image of Fe₂O₃-TiO₂.

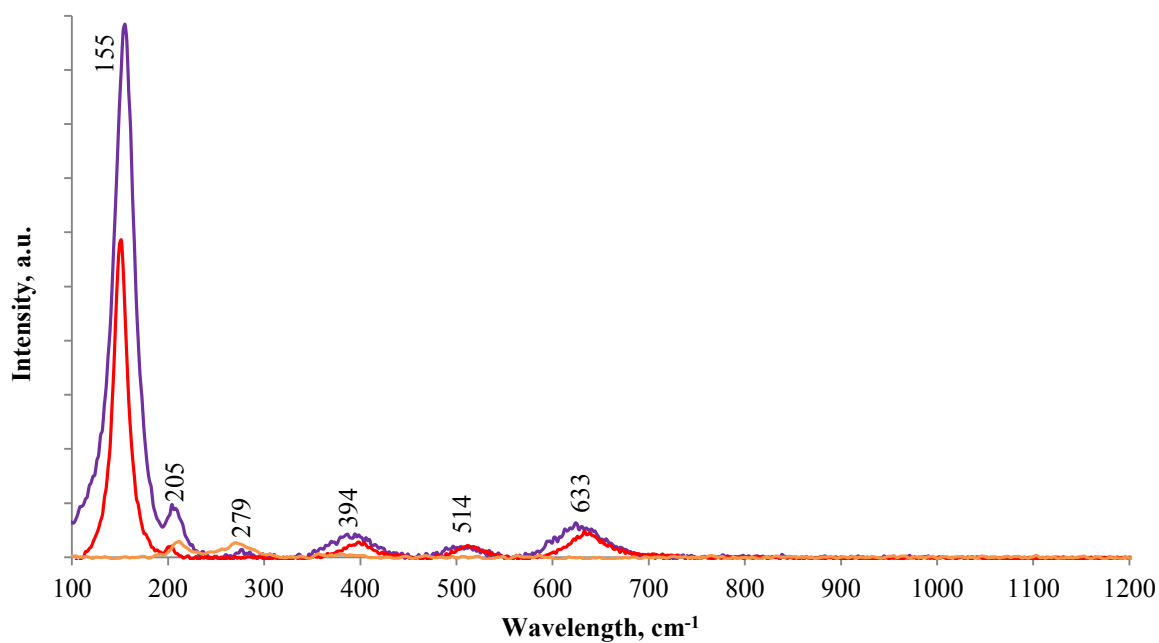


Fig. 13. Raman spectra of Fe₂O₃-TiO₂ (purple), P25 (red), and Fe₂O₃ (brown).

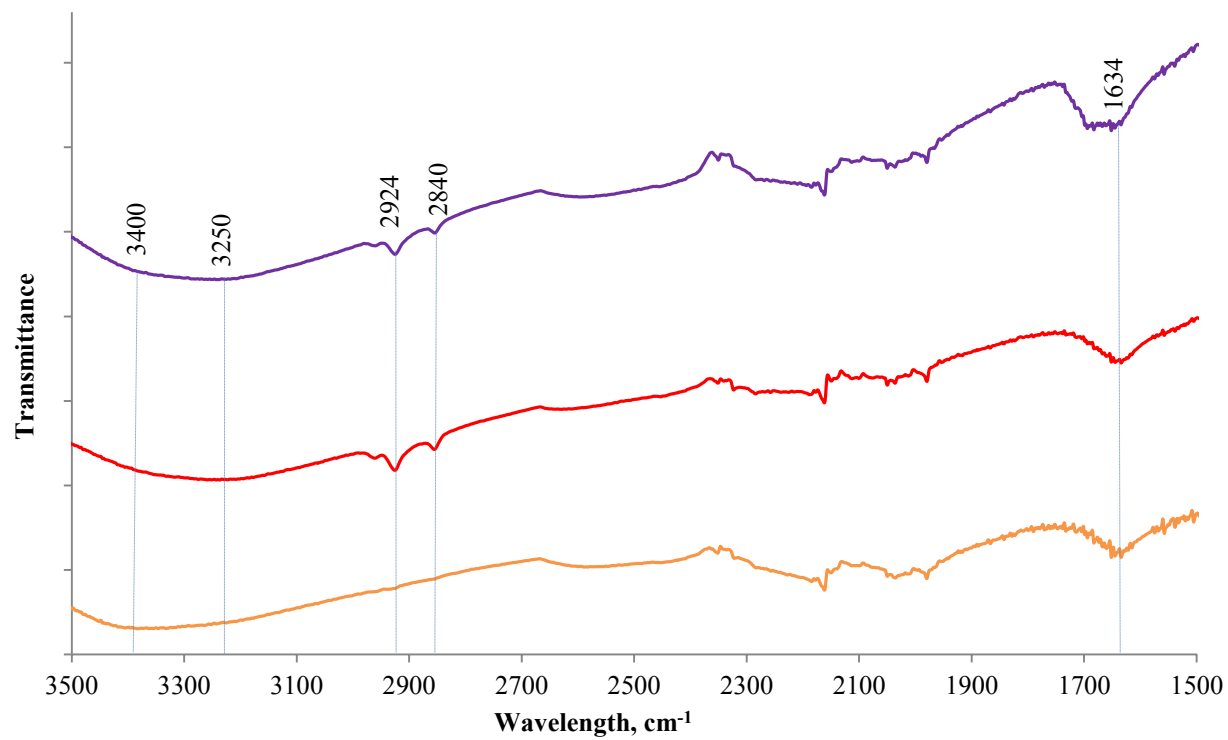


Fig. 14. FTIR spectra of Fe₂O₃-TiO₂ (purple), P25 (red), and Fe₂O₃ (brown).

List of Tables

Table 1

Comparison of catalyst characteristics among Fe₂O₃-TiO₂, P25 and Fe₂O₃.

Sample	XRD Crystallite size, nm	Surface analysis			Band gap energy, eV
		Specific surface area, m ² /g	Pore volume, cm ³ /g	Pore size, nm	
Fe ₂ O ₃ -TiO ₂ *	22.99	58.40	0.29	18.52	2.95
P25	24.29	52.32	0.17	15.62	3.35
Fe ₂ O ₃	17.45	7.70	0.03	13.14	1.60

*Mechanochemical synthesis conditions: milling speed =250 rpm; [Fe₂O₃] =1 mol%;
ball:powder mass ratio =10:1

Table 2

Textural properties of Fe₂O₃-TiO₂ at different milling time.

Milling time, min	Surface analysis		
	Specific surface area, m ² /g	Pore volume, cm ³ /g	Pore size, nm
10	55.57	0.26	16.16
15	56.99	0.28	17.22
20	58.40	0.29	18.52
25	55.18	0.24	15.29
30	52.41	0.22	15.00

Mechanochemical synthesis conditions: milling speed =250 rpm; [Fe₂O₃] =1 mol%; ball:powder mass ratio =10:1

Table 3

Crystallite properties of Fe₂O₃-TiO₂ at different milling speed.

Milling speed, rpm	XRD analysis	
	Crystallite size, nm	Rutile phase fraction, %
150	25.72	0.29
200	24.05	0.29
250	22.99	0.36
300	22.00	0.38
350	21.42	0.44

Mechanochemical synthesis conditions: milling time =20 min; [Fe₂O₃] =1 mol%; ball:powder mass ratio =10:1

Table 4

Control photocatalytic experiments.

Control	COD removal, %
Photolysis	0.1
Catalysis (in the dark using Fe ₂ O ₃ -TiO ₂)	0.4
P25	40.6
Anatase TiO ₂	24.9
Rutile TiO ₂	2.9
Fe ₂ O ₃	1.1